Arabian Journal of Chemistry (2022) **15**, 103934

King Saud University

Arabian Journal of Chemistry

www.ksu.edu.sa
www.sciencedirect.com

ORIGINAL ARTICLE

A pH-response multifunctional nanoplatform based on $NaGdF_4$:Yb,Er,Fe@Ce6@$mSiO_2$-DOX for synergistic photodynamic/chemotherapy of cancer cells

Yue Zhao [a,b,1], Enlv Hong [c,d,e,1], Lumin Liu [a,b,1], Zhao Chen [a,b], Jianwei Zhang [a,b], Yang Wu [a], Xiaoyu Linghu [a,b], Yue Shu [a,b], Dan Shan [a,b], Baiqi Wang [a,b,f,*]

[a] *Department of Occupational and Environmental Health, School of Public Health, Tianjin Medical University, Tianjin 300070, China*
[b] *Tianjin Key Laboratory of Environment, Nutrition and Public Health, Tianjin 300070, China*
[c] *Department of Infection Management, Tianjin Medical University Cancer Institute and Hospital, National Clinical Research Center for Cancer, Tianjin 300202, China*
[d] *Key Laboratory of Cancer Prevention and Therapy, Tianjin 300202, China*
[e] *Tianjin's Clinical Research Center for Cancer, Tianjin 300202, China*
[f] *National Demonstration Center for Experimental Preventive Medicine Education (Tianjin Medical University), Tianjin 300070, China*

Received 23 January 2022; accepted 17 April 2022
Available online 22 April 2022

KEYWORDS

$NaGdF_4$:Yb,Er,Fe;
Nanoplatform;
Combined therapy;
Photodynamic therapy;
Cancer cells;
pH response

Abstract Cancer is one of the major diseases that seriously threaten human health. Drug delivery nanoplatforms for tumor treatment have attracted increasing attention owing to their unique advantages such as good specificity and few side effects. This study aimed to fabricate a pH-responsive drug release multifunctional nanoplatform $NaGdF_4$:Yb,Er,Fe@Ce6@$mSiO_2$-DOX. In the platform, Fe^{3+} doping enhanced the fluorescence intensity of $NaGdF_4$:Yb, Er by 5.8 folds, and the $mSiO_2$ shell substantially increased the specific surface area of nanomaterials (559.257 m^2/g). The loading rates of chlorin e6 and doxorubicin hydrochloride (DOX) on $NaGdF_4$:Yb,Er,Fe@Ce6@$mSiO_2$-DOX reached 28.58 ± 0.85% and 87.53 ± 5.53%, respectively. Additionally, the DOX release rate from the nanoplatform was only 24.4% after 72 h at pH 7.4. However, under tumor microenvironment conditions (pH 5.0), the release rate of DOX increased to 85.3% after 72 h. The nanoplatform could generate reactive oxygen species (ROS) under 980 nm near-

* Corresponding author at: No. 22, Qixiangtai Rd., Heping Dist., Tianjin 300070, China.
E-mail address: wangbaiqi@tmu.edu.cn (B. Wang).
[1] These authors contributed equally to this work.
Peer review under responsibility of King Saud University.

Production and hosting by Elsevier

https://doi.org/10.1016/j.arabjc.2022.103934

infrared excitation. Moreover, the nanoplatform exhibited a strong comprehensive killing efficiency against cancer cells. The viabilities of HeLa, MCF-7, and HepG2 cancer cells were only 18.5, 11.4, and 9.3%, respectively, after being treated with a combination of photodynamic therapy and chemotherapy. The constructed nanoplatform exhibits great application potential in cancer treatment.

1. Introduction

Cancer is one of the serious diseases threatening human life. According to statistics from the International Agency for Research on Cancer, there were approximately 19.3 million new cancer cases and nearly 10 million cancer deaths worldwide in 2020 (Sung et al., 2021). It is estimated that by 2030, the number of new cancer cases will reach 22.2 million and the number of death cases would reach approximately 13.2 million (Bray et al., 2012). The traditional methods for clinical treatment of cancer include chemotherapy, radiotherapy, and surgical resection. However, these methods are not effective for malignant tumors. The 5-year survival rate is still low and usually accompanied by serious side effects (Nagasubramanian et al., 2003). Therefore, it is extremely important to develop drug delivery systems that have very few side effects and high selectivity for cancer cells and can be used continuously. For this reason, many scientists are working hard to develop agents that can deliver therapeutic chemicals to target tumor sites without damaging healthy cells (Li et al., 2021; Zhang et al., 2021; Zhang et al., 2022; Zhou et al., 2020).

In recent years, rare-earth-doped up-conversion nanoparticles (UCNPs) have attracted attention owing to their ability to convert low-energy near-infrared (NIR) photons into high-energy visible light or ultraviolet light emission. Additionally, the high biocompatibility (Grzyb et al., 2015) of UCNPs facilitates the wide use of this material in the biomedical field, including nano-level biotags (Li et al., 2013; Shen et al., 2014; Wu et al., 2013; Zhang et al., 2018), nano-drug carriers (Xu et al., 2014), and tumor imaging and treatment (Deng et al., 2014; Liu et al., 2016; Teng et al., 2018; Yin et al., 2014; Zhou et al., 2014). However, application of UCNPs in the biological field largely depends on the degree of surface modification and functionalization. The synthesized UCNPs are usually end-capped with organic ligands; hence, they are insoluble in water. The UCNPs can be used for subsequent biological applications only after hydrophilic treatment of their surface. Therefore, surface modification is a key step in the manufacture of UCNP-based bioprobes for various biomedical applications.

Mesoporous silica nanomaterials exhibit excellent biocompatibility at a concentration suitable for pharmacological applications (Cho et al., 2017; Slowing et al., 2007). In addition, mesoporous silica nanomaterials also have a variety of unique and advantageous structural characteristics, such as high specific surface area, high pore volume, stable mesoscopic structure, adjustable pore size, and two functional surfaces that can be modified (external particles and internal pore surface) (Gui et al., 2017; Liu et al., 2021). The large specific surface area and pore volume of the material can increase drug loading. The highly ordered pore structure enables the control of the diffusion and release of drug molecules within the target area, thereby reducing the total dose and preventing acute or chronic complications (Vivero-Escoto et al., 2010). Mesoporous silica nanomaterials can be effectively endocytosed by a variety of cell lines. Cellular intake can be controlled by different factors, such as the size and morphology of the nanoparticles, the electrostatic interaction with the cell membrane, and the surface functionalization of nanoparticles (Lu et al., 2009; Trewyn et al., 2008). Moreover, by using the "Gatekeeper" molecule, the drug can be sealed in the pore and can be released only under the action of specific exogenous or endogenous stimuli (such as the acidic micro environment of the tumor) to achieve controlled drug release. These advantages of mesoporous silica nanomaterials make them an ideal surface modifier for up-conversion nanomaterials.

The pH of most cancer tissues is lower than that under normal physiological conditions (pH 7.4), and the decline in pH within the cell is greater (especially the pH value in the endosome can reach 4.5) (Dong et al., 2018; Gui et al., 2017). If the drug delivery system could be "smart"-controlled based on the specific local tumor microenvironment, it would enable target therapy and aid in avoiding side effects in cancer treatment. Numerous studies have demonstrated that pH-sensitive controlled-release systems exhibit outstanding performance in the field of tumor treatment (Lu et al., 2007). In addition, among various anti-cancer drugs, DOX is an effective water-soluble antibiotic and is used as a first-line treatment for a variety of cancers. Although some groups reported the use of pH-responsive microporous silica as anti-cancer drug carriers, the fabrication of these systems is generally complicated and difficult to widely apply in practice. Hence, there is an urgent need to develop a new synthesis approach and drug delivery system to meet practical requirements.

In addition, UCNPs with strong up-conversion fluorescence (UCL) properties are the foundation of UCNP nanoplatforms. Numerous studies have demonstrated that doping UCNPs with heterovalent impurity ions can effectively tune their fluorescence properties. Among numerous ions, the Fe^{3+} ion has been widely used to improve the UCL intensity of nanomaterials (Chuai et al., 2015; Ramasamy et al., 2013; Tang et al., 2015; Wei et al., 2019). However, how Fe^{3+} ions adjust the UCL of UCNPs has been seldom reported.

In this study, Fe^{3+}-doped $NaGdF_4$:Yb,Er UCNPs were capped with microporous silica materials to build a UCNPs@$mSiO_2$ core-shell structured nanocomposite. Then, the photosensitizer chlorin e6 (Ce6) and the chemotherapeutic drug DOX were loaded to construct the $NaGdF_4$:Yb,Er,Fe@Ce6@$mSiO_2$-DOX nanoplatform. DOX contains amino groups that are positively charged under physiological conditions. DOX can combine with negatively charged DNA to play an anti-cancer role. Based on this principle, we designed a DOX drug delivery nanoplatform. After the surface of UCNPs@Ce6@mSiO2 nanoparticles is carboxylated, the negative charge of the pore surface nanoplatform increases. The electrostatic interaction between the nanoplatform and DOX increases. This promotes the effective loading of DOX. Under physiological conditions (pH = 7.4), carboxyl groups on the nanoplatform and DOX can maintain the electrostatic interaction and effectively upload and deliver an anti-cancer drug. However, in the tumor microenvironment with low pH, the electrostatic interaction between nanoparticles and DOX decreases and the electrostatic repulsion increases. This triggers the release of DOX from nanocarriers. This is of great significance for the clinical application of the nanoplatform.

Liver cancer is the second leading cause of cancer-related deaths worldwide after lung cancer, and breast cancer and cervical cancer are the most common female cancers currently. Therefore, HeLa, MCF-7, and HepG2 were chosen as the representatives of cancer cells. The cells were treated with the fabricated $NaGdF_4$:Yb,Er, Fe@Ce6@$mSiO_2$-DOX nanoplatform. Under 980 nm near-infrared irradiation (NIR), the nanoplatform could effectively generate reactive oxidative species (ROS) and release DOX in the tumor microenvironment with a low pH. Furthermore, the nanoplatform exhibited the perfect combined therapeutic effect for photodynamic therapy (PDT)

and chemotherapy. The developed nanoplatform shows a great application potential for the combined PDT/chemotherapy in tumor treatment.

2. Methods and materials

2.1. Materials and chemicals

All chemical reagents used in this study were of analytical grade and used without further purification. $Gd(NO_3)_3{\cdot}6H_2O$ (99.99%), cetyltrimethylammonium bromide (CTAB) (98%), aminopropyltriethoxy silane (APTES) (99%), and TEOS (98%) were purchased from Xiensi Biochemical Technology Co., Ltd (Tianjin, China). $Yb(NO_3)_3{\cdot}5H_2O$ (99.9%), $Er(NO_3)_3{\cdot}5H_2O$ (99.9%), cyclohexane, and anhydrous ethanol (99.7%) were obtained from Sigma-Aldrich (Germany). NaOH (96%), NH_4F (98%), oleic acid (OA), $FeCl_3{\cdot}6H_2O$ triethylamine and N,N-dimethylformamide (DMF) were obtained from Kermel Chemical Reagent Co., Ltd (Tianjin, China). EDC-HCl and NHS were purchased from Sinopharm Chemical Reagent Co., Ltd (Shanghai, China). NH_4NO_3 was obtained from Hongxing Chemical Reagent Co., Ltd (Beijing, China). DOX was purchased from MedChemExpress (Shanghai, China), Ce6 was purchased from J&K Scientific Ltd. (Beijing, China), and succinic anhydride (98%) was obtained from Macklin Chemical Reagent Co., Ltd (Shanghai, China).

2.2. Fabrication of the UCNP@Ce6@mSiO_2-DOX nanoplatform

2.2.1. Preparation of $NaGdF_4$:20 mol% Yb,2mol% Er,xmol% Fe UCNPs

$NaGdF_4$:Yb,Er,Fe UCNPs were synthesized via a one-step hydrothermal method using OA as the coordinating ligand. In a typical synthesis, 0.7 g (17.5 mmol) NaOH, 8 mL (25 mmol) OA, and 12 mL (206 mmol) anhydrous ethanol were mixed under agitation to form a white viscous solution. Following this, 4.8 mmol NH_4F (dissolved in 8.5 mL deionized water) was added to the above-mentioned solution and stirred to form a transparent solution. Then, 1.2 mL of an $Ln(NO_3)_3$ solution (0.8 M, Ln: 58 mol% Gd; 20 mol% Yb; 2 mol% Er) and 0 mol%,10 mol% or 20 mol% $FeCl_3$ solution was added under vigorous stirring. The mixture was then agitated for another 20 min at room temperature (~25 °C) to form a translucent colloidal solution. Subsequently, 30 mL of the mixed solution was transferred to a Teflon-lined high-pressure reactor, and the system was kept at 180 °C for 12 h. After naturally cooling to room temperature, the sample was centrifuged at 2000 rpm for 3 min, washed with cyclohexane and ethanol alternately thrice, and then dispersed in cyclohexane for the subsequent experiments.

2.2.2. Preparation of UCNPs@Ce6@mSiO_2

The Stober method was used to coat the silica shell. The synthesized UCNPs were dissolved in cyclohexane (10 mg in 2 mL) and added to 20 mL of an aqueous solution containing 100 mg CTAB. The solution was stirred vigorously overnight at room temperature to evaporate cyclohexane. Then, 10 mL distilled water, 3 mL ethanol, and 150 μL NaOH solution (2 M) were added and heated to 70 °C while stirring. When the temperature was stable, a pretreated Ce6 solution (2 mg dissolved in 0.5 mL DMSO containing 12 μL APTES, 6 mg EDC-HCl, 4 mg NHS) was added and allowed to react at 37 °C for 2 h, following which 120 μL TEOS was added dropwise into the solution, which was kept at 70 °C for 2 h. After cooling to room temperature, the resulting nanocomposite was centrifuged at 3000 rpm for 5 min and washed with ethanol three times. Subsequently, the surfactant CTAB was removed using the ion exchange method. The obtained UCNPs@Ce6@mSiO_2 nanocomposite was dispersed in 50 mL of an ethanol solution containing 0.3 g NH_4NO_3 and stirred at 60 °C for 24 h. Finally, the sample was centrifuged and washed three times with ethanol to remove the remaining CTAB and then dispersed in ethanol. Finally, the sample was centrifuged and washed thrice with ethanol and then dispersed in ethanol. The filtrate was collected to measure the Ce6 content via UV–vis spectroscopy.

2.2.3. Preparation of UCNPs@Ce6@mSiO_2-COOH

First, 100 mg of UCNPs@Ce6@mSiO_2 was added to 100 mL of ethanol and sonicated for 10 min to establish uniform dispersion. Then, 3 mL APTES was added and the solution was transferred to a 50 °C water bath and stirred for 24 h. The reaction product (amino-modified UCNPs@Ce6@mSiO_2) was collected via centrifugation and washed with ethanol. Next, 50 mg amino-modified UCNPs@Ce6@mSiO_2, 40 mg succinic anhydride, and 60 μL triethylamine were dispersed in 5 mL DMF and allowed to react at 40 °C for 24 h. After centrifugation and ethanol wash, the carboxyl-modified UCNPs@Ce6@mSiO_2 was obtained.

2.2.4. Preparation of UCNPs@Ce6@mSiO_2-DOX

DOX (3 mL, 1 mg/mL) was mixed with UCNPs@Ce6@mSiO_2 in phosphate-buffered saline (PBS) to load DOX onto UCNPs@Ce6@mSiO_2. After stirring overnight at 37 °C, UCNPs@Ce6@mSiO_2@DOX was separated via centrifugation and gently washed thrice with PBS. The filtrate was collected to measure DOX content via UV–vis spectroscopy.

2.3. Characterization

A Thermo Scientific ESCALAB 250Xi X-ray photoelectron spectrometer was used to analyze the sample; a Rigaku-Dmax 2500 X-ray powder diffractometer (operating at 40 kV and 200 mA current settings) was used to analyze the sample in the crystalline phase using Cu-Kα radiation (1.54056 Å); a HITACHI HT 7700 transmission electron microscope (TEM) was used to observe the morphology of the sample. A Kanta Automatic gas adsorption analyzer was used to analyze the specific surface area, pore volume, and pore diameter of the sample; a Thermo Scientific Fourier transform infrared spectrometer was used to obtain the infrared spectrum. A HITACHI U-3900 ultraviolet–visible spectrophotometer was used to obtain the ultraviolet–visible absorption spectrum of the sample, and a HITACHI F-2500 fluorescence spectrophotometer was used to obtain the UCL spectrum of the sample.

2.4. Loading contents of Ce6 and DOX

The subtraction method was used to calculate the loading rates of Ce6 and DOX. The standard curves of Ce6 and DOX are

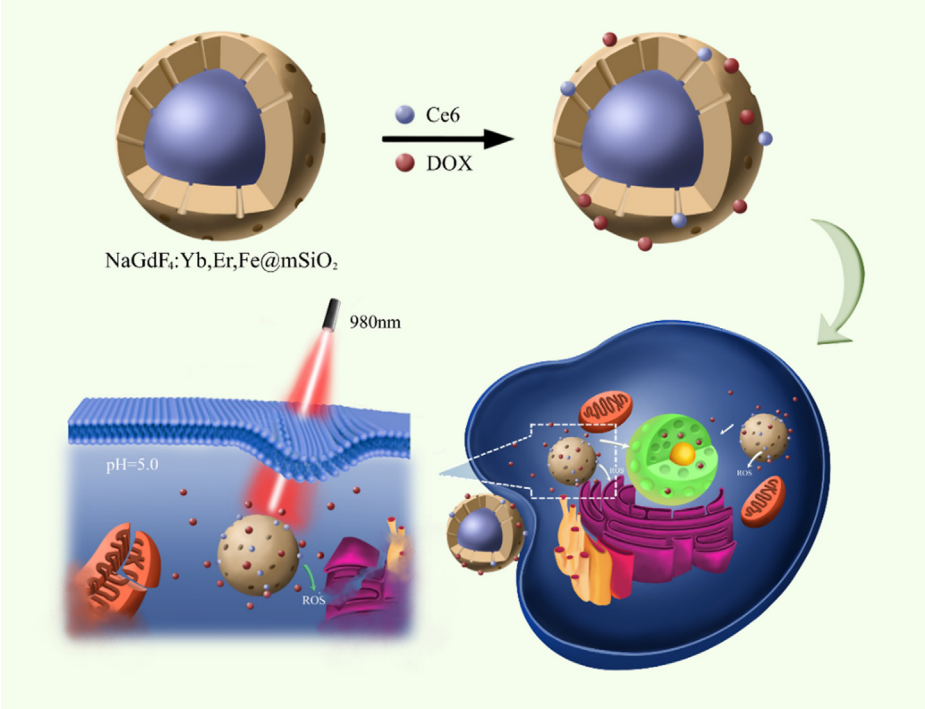

Fig. 1 Schematic of the fabricated nanoplatform in combined PDT-chemotherapy.

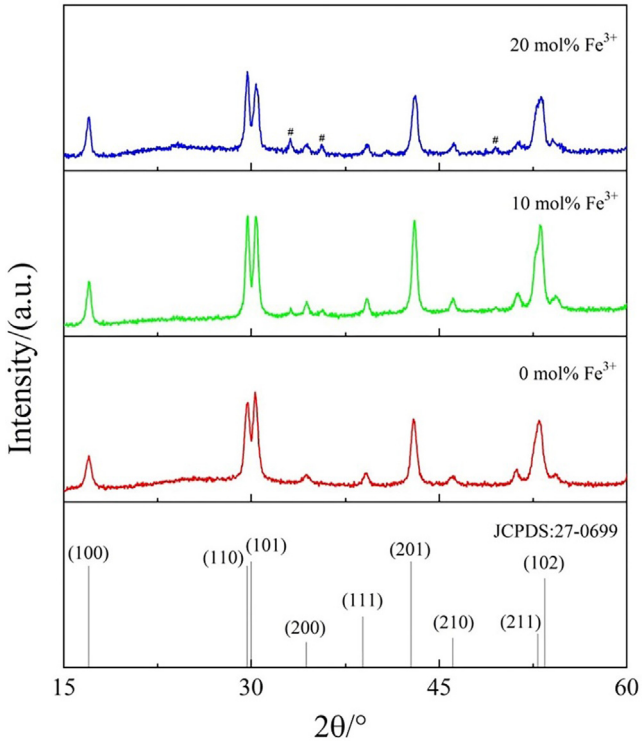

Fig. 2 XRD patterns of $NaGdF_4$:Yb,Er nanoparticles doped with 0, 10, or 20 mol% Fe^{3+} (# - hexagonal Fe_2O_3).

depicted in Fig. S1 and S2. Briefly, the UCNPs were added dropwise into a Ce6 solution (2 mg dissolved in 0.5 mL DMSO containing 12 µL APTES, 6 mg EDC-HCl, 4 mg NHS) at 70 °C for 2 h. The mixture was centrifuged at 3000 rpm for 5 min and washed thrice. The filtrate was collected, and absorbance was measured at 404 nm. Through the standard curve, the amount of Ce6 in the filtrate was calculated. The initial mass of 2 mg was subtracted from the amount determined in the filtrate to obtain the amount of Ce6 loaded onto the nanoplatform, referred to as the loading efficiency. The experiment was repeated thrice, and the results obtained were averaged. The loading rate of Ce6 was derived using the following equation:

$$\text{Loading Efficiency } (\%) = \frac{m_o - m_f}{m_o} \times 100\%$$

where m_o is the original mass of Ce6 or DOX in $UCNPs@Ce6@mSiO_2$ or $UCNPs@Ce6@mSiO_2$-DOX and m_f is the mass of the substance in the filtrate. The experimental procedure and calculation of the DOX loading rate were the same as for Ce6, and the maximum absorption peak of DOX was 480 nm.

2.5. pH-responsive DOX release

The pH-triggered drug release was tested via adding 20 mg of $UCNPs@Ce6@mSiO_2$-DOX to 5 mL PBS at pH 7.4 or 5.0 in a dialysis bag (molecular weight cut off = 8 kDa), which was placed in 40 mL respective buffer solutions, and stirred at 37 °C. After 0, 1, 2, 3, 4, 5, 7, 9, 24, 48, and 72 h, 5 mL of buffer solution was removed and 5 mL of fresh buffer solution was added. The amount of released DOX was analyzed via UV–vis spectroscopy.

2.6. ROS generation in solution

A photochemical method with 1,3-diphenylisobenzofuran (DPBF) was used to detect singlet oxygen. DPBF (50 µL, dis-

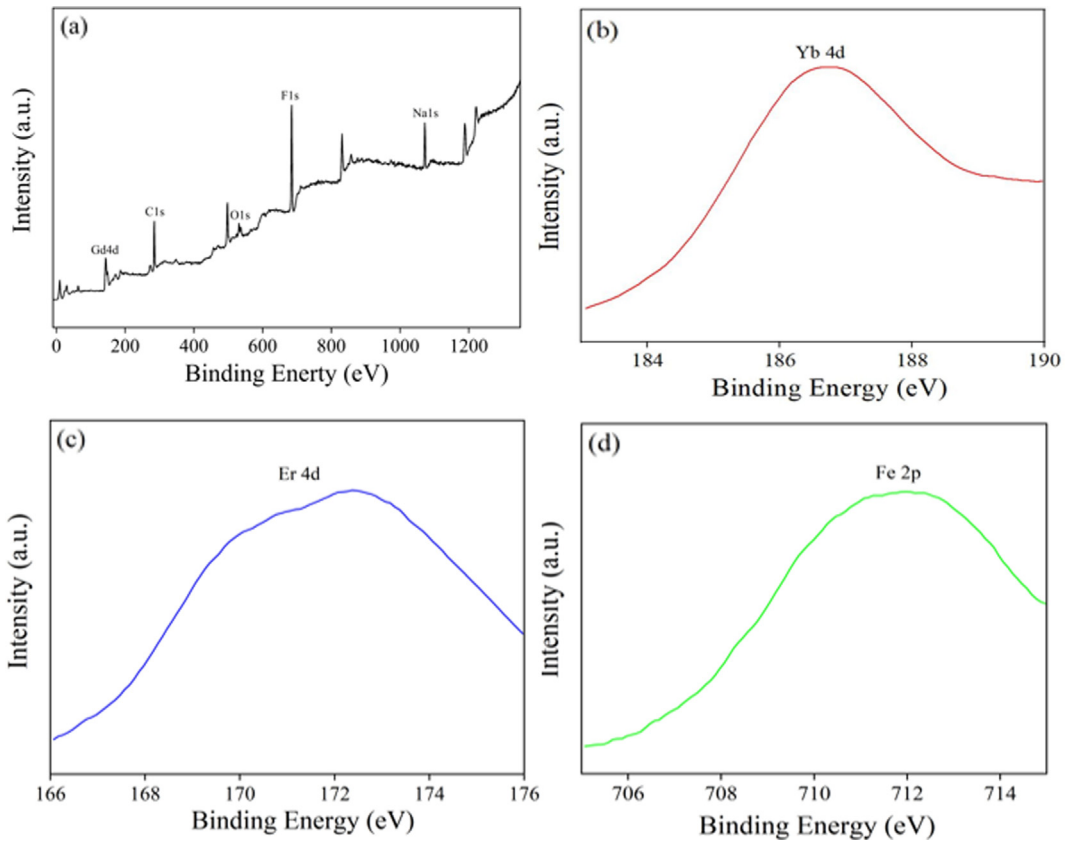

Fig. 3 XPS of 20 mol% Fe^{3+}-doped $NaGdF_4$:Yb,Er nanoparticles. (a) Survey, (b) Yb 4d, (c) Er 4d, and (d) Fe 2p.

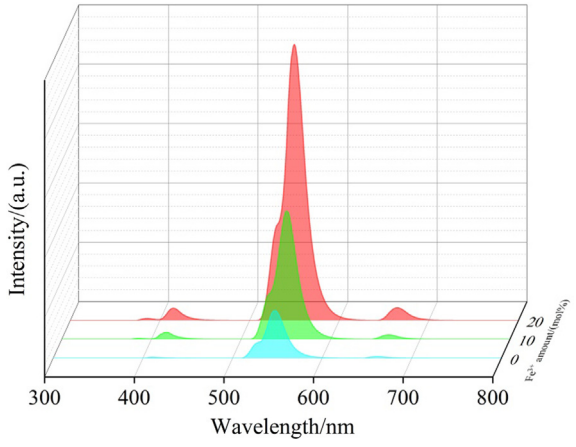

Fig. 4 Fluorescence spectra of $NaGdF_4$:Yb,Er nanoparticles doped with 0, 10, or 20 mol% Fe^{3+} under 980 nm excitation.

solved in ethanol, 1.5 mg/mL) was added to 2 mL of the UCNP@Ce6@mSiO_2 (dissolved in ethanol, 1.0 mg/mL) solution. The mixture was exposed to NIR at 980 nm, and the fluorescence emission of DBPF (440 nm excitation light source) was recorded at different time points (1, 3, 5, 10, 15 min).

2.7. Cytotoxicity assay

Human cervical cancer HeLa cells (8,000 cells per well), human breast cancer MCF-7 cells (6,000 cells per well), and human liver cancer HepG2 cells (8,000 cells per well) were seeded onto a 96-well plate, respectively, for 24 h. The nanomaterials were dissolved in a culture medium without fetal bovine serum (FBS). To improve the solubility of UCNPs, 5 vol% of DMSO was added to the incomplete culture medium. The cells were incubated in different solutions with various concentrations of UCNPs. For the experimental group, after the nanoparticles were incubated for 4 h, the 96-well plates were irradiated at 980 nm (2 W/cm^2) for 10 min (1 min interval after every 1 min irradiation). After 24 h, 20 μL of MTT solution (5 mg/mL MTT in PBS, pH 7.4) was added to each well, and the plate was incubated for an additional 4 h. After 4 h of incubation, the solution in the well was replaced with 150 μL DMSO and the plate was shaken for 10 min. The absorbance was recorded at 490 nm using a BioTek Synergy MX multifunctional enzyme labeler and cell viability was calculated from the average value of six parallel wells. Each experiment was repeated thrice. The following formula was applied to calculate the percentage inhibition of cell growth:

Cell viability (%) = (mean of absorbance value of treatment group/mean of absorbance value of control) × 100%.

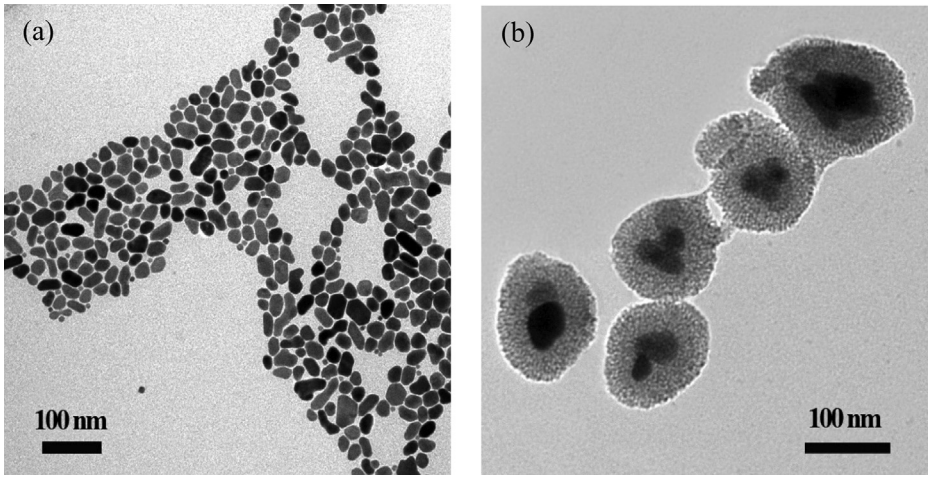

Fig. 5 TEM images of (a) UCNPs and (b)UCNPs@mSiO$_2$.

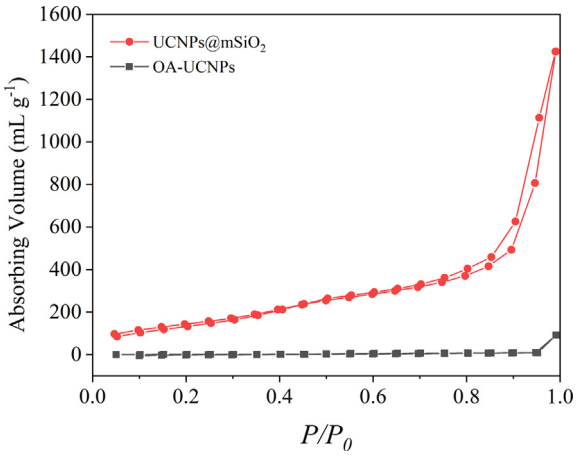

Fig. 6 Nitrogen adsorption-desorption curves of OA-UCNPs and UCNPs@mSiO$_2$.

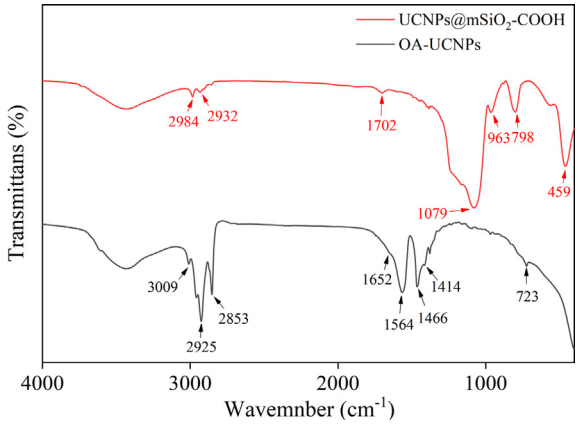

Fig. 7 FTIR spectra of OA-UCNPs and UCNPs@mSiO$_2$-COOH nanoparticles.

2.8. Statistical methods

GraphPad-Prism software was used to draw graphs and perform data analysis. ANOVA and Dunnett multiple comparison test were used to compare groups and measure the *P*-value. $P < 0.05$ was considered statistically significant. (See Fig. 1)

3. Results and discussion

3.1. Characterization of Fe^{3+}-doped $NaGdF_4$:Yb,Er

3.1.1. Analysis of the crystal structure

Fig. 2 shows the X-ray diffraction (XRD) patterns of nanoparticles doped with different amounts of Fe^{3+}. The samples exhibited three main diffraction peaks at 29.74°, 30.32°, and 42.92°, which can be attributed to (110), (101), and (201) facet diffraction of β-$NaGdF_4$ crystals, respectively, (JCPDS: 27-0699). Because of Fe^{3+} doping, hexagonal Fe_2O_3 diffraction peaks appear at 33.14°, 35.64° and 49.48°, which correspond to (104), (110) and (024) facets, respectively, (JCPDS: 33-0664). When Fe^{3+} content reached 10 mol%, the crystallinity of β-$NaGdF_4$ was enhanced. However, upon increasing the Fe^{3+} content further, the crystallinity of β-$NaGdF_4$ decreased. It was probably because Fe^{3+} ions were substituted for Gd^{3+} ions in UCNPs (Ramasamy et al., 2013). When Fe^{3+} doping was relatively low (10 mol%), the Fe^{3+} ions seemed beneficial for β-$NaGdF_4$ crystallization. However, with a further increase in Fe^{3+} content, the crystallization of β-$NaGdF_4$ was inhibited. In addition, it is noteworthy that the growth rate of the $NaGdF_4$ (110) facet remarkably increased with the increase in Fe^{3+} content. This phenomenon is probably due to the lattice distortion caused by Fe^{3+} doping, which was also observed by Ramasamy (Ramasamy et al., 2013).

3.1.2. Elemental analysis

XPS was used to determine the elemental composition of the synthesized samples. Fig. 3a shows the survey XPS spectrum of 20 mol% Fe^{3+} ion-doped nanomaterials. The binding energies of Na 1s and F 1s appeared at 1072.44 eV and 685.05 eV;

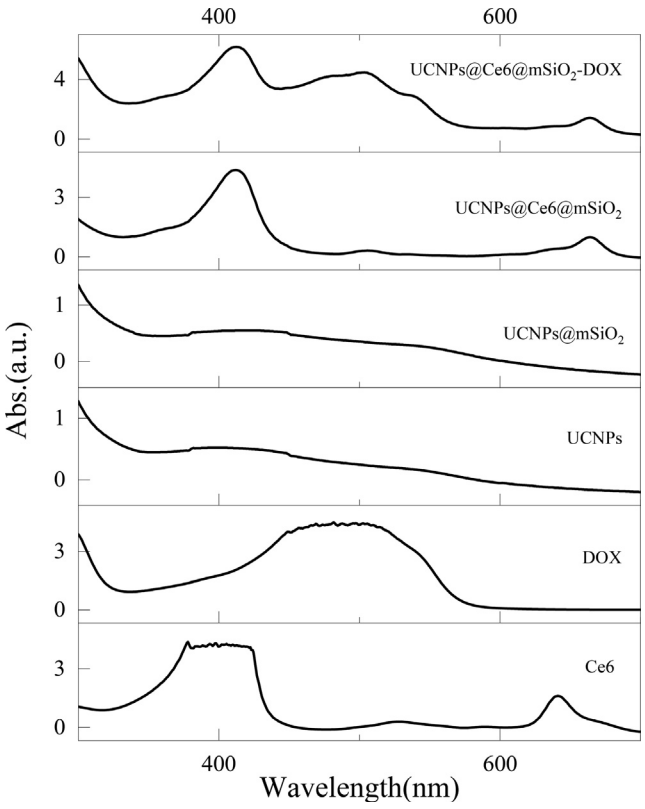

Fig. 8 UV–visible absorption spectra of Ce6, DOX, UCNPs, UCNPs@$mSiO_2$, UCNPs@Ce6@$mSiO_2$, and UCNPs@Ce6@$mSiO_2$-DOX.

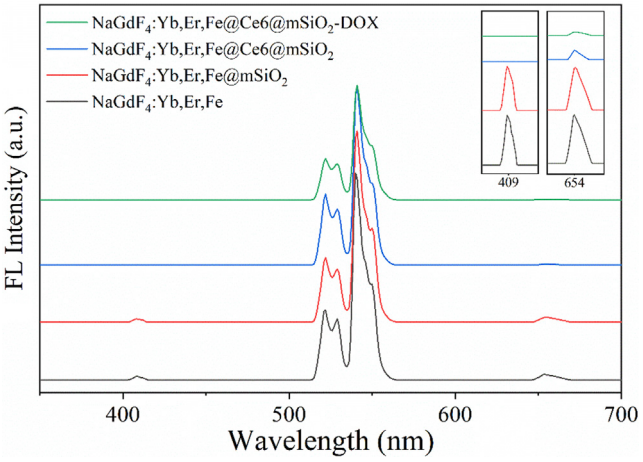

Fig. 9 UCL spectrum of the synthesized nanoplatforms under 980 nm laser excitation.

the peaks located at 149.17 eV and 142.97 eV can be attributed to Gd $4d_{3/2}$ and Gd $4d_{5/2}$ binding energy, respectively. These three elements constituted the β-$NaGdF_4$ host matrix. Figs. 3b and 2c show the binding energies of Yb 4d and Er 4d, wherein the peaks were located at 186.47 eV and 172.87 eV, respectively. This demonstrated that $NaGdF_4$:Yb, Er nanomaterials were doped with Yb and Er. In addition, the peaks at 711.87 eV, shown in Fig. 3d, were attributed to the Fe $2p_{3/2}$ binding energy. This confirms the successful Fe^{3+} doping in $NaGdF_4$:Yb,Er nanoparticles (Ramasamy et al., 2013).

3.1.3. UCL analysis

Fig. 4 shows the fluorescence spectra of $NaGdF_4$:Yb,Er nanoparticles doped with different amounts of Fe^{3+} ions under 980 nm laser excitation. The main emission peaks appeared at 415, 530, 550, and 665 nm, which were attributed to the $^2H_{9/2}$-$^4I_{15/2}$, $^2H_{11/2}$-$^4I_{15/2}$, $^4S_{3/2}$-$^4I_{15/2}$, and $^4F_{9/2}$-$^4I_{15/2}$ energy transitions of Er^{3+} ions, respectively (Bai et al., 2007; Vetrone et al., 2009). The fluorescence intensity of the nanoparticles was enhanced when the content of Fe^{3+} ions increased. The UCL intensity of 10 and 20 mol% Fe^{3+}-doped $NaGdF_4$:Yb,Er nanoparticles at 550 nm increased by 2.7 and 5.8 folds compared with that of the Fe^{3+}-free sample. It is well known that the UCL intensity of rare-earth ions is mainly dependent on electron transition probabilities, and a hypersensitive transition can be triggered by changing environment. Thus, this obvious enhancement in UCL intensity might be induced by Fe^{3+} ions with a small radius, which can tailor the surrounding environment around the Er^{3+} ions in the crystal, leading to hypersensitive transition (Ramasamy et al., 2013). Therefore, a certain amount of Fe^{3+} ions doping could effectively enhance the fluorescence efficiency of $NaGdF_4$:Yb, Er nanoparticles. Based on UCL, 20 mol% Fe^{3+}-doped $NaGdF_4$:Yb,Er nanoparticles were chosen as core structure in the following experiments.

3.2. Characterization of the nanoplatform

3.2.1. Morphology analysis

As shown in Fig. 4a, $NaGdF_4$:Yb,Er,Fe nanoparticles were ellipsoidal with a size of approximately 25 nm. After the UCNPs were coated with silica, the particles exhibited good dispersion and a quasi-spherical shape, and the particle size was approximately 100–150 nm. The average for UCNP@$mSiO_2$ was approximately 130 nm. Each core-shell nanoparticle had one or more UCNP core, and the silica layer was uniformly coated on the surface of the nanoparticle at a thickness of approximately 50 nm. It is worth noticing that the pore structure could be clearly observed (Fig. 5b). This indicated that the silica layer was successfully coated on the surface of the UCNPs and possibly formed a mesoporous structure.

3.2.2. Specific surface area and pore size analyses

To further clarify the specific surface area and pore size distribution of the mesoporous silicon layer, as well as obtain nitrogen adsorption-desorption isotherms, nitrogen adsorption and desorption experiments were performed on UCNPs and UCNP@$mSiO_2$ nanoparticles. It is obvious from Fig. 6 that the physisorption isotherm of UCNP@$mSiO_2$ could be classified as type V, confirming the existence of the mesoporous structure (Jiang et al., 2014; Tian et al., 2019). This was also in agreement with previous results. The specific surface area of the nanoparticles coated with silica was significantly higher

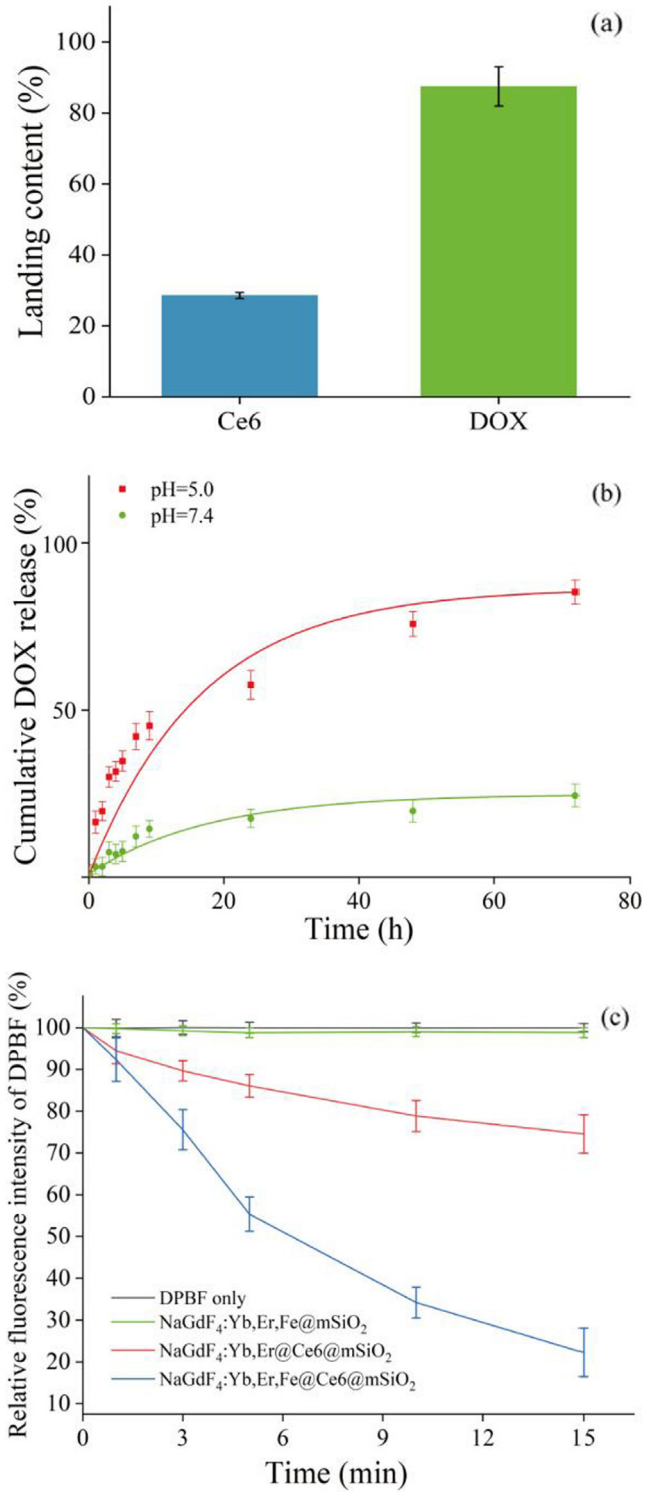

Fig. 10 a) Ce6 and DOX loading. (b) Cumulative DOX release (pH = 5.0, 7.4). (c) Degradation curve of DPBF under NIR irradiation.

than that of the nanoparticles without the silicon coating ($P < 0.01$). The specific surface area of the nanomaterials rapidly increased from 5.149 m^2/g to 559.257 m^2/g. UCNPs@SiO_2 had a pore volume of 2.192 mL/g and a pore diameter of 3.087 nm, as calculated using the BJH model. These findings demonstrated that the nanocomposite material formed a porous structure after silica coating.

3.2.3. Chemical bond analysis

The Stober method was used to coat the surface of $NaGdF_4$:Yb,Er,Fe nanoparticles with mesoporous silica, which greatly increased the specific surface area and pore volume. Since there are a large number of hydroxyl groups on the surface of pores and the silica layer, we further modified the amino groups using APTES, and with the aid of the ring cleavage of succinic anhydride, carboxyl groups were attached to the surface of the particles based on the amino modification.

To clarify the $mSiO_2$ and carboxyl group modifications of the UCNP surface and analyze the chemical bonds on the surface of the nanoparticles, FTIR was used; the results are shown in Fig. 7. In the FTIR spectrum of OA-UCNPs, the absorption peak at 3009 cm^{-1} originated from the C—H vibration of the alkenyl group, while the weak absorption peak at 1652 cm^{-1} was attributed to the alkenyl C═C vibration. The absorption peaks at 2925, 2853, 1466, and 723 cm^{-1} were attributed to the asymmetric vibration, symmetric vibration, "scissor swing", and "Swing" vibration of C—H in the alkyl group, respectively. The absorption peaks of 1564 and 1414 cm^{-1} were the stretching vibration peaks of the carboxyl group —COO— in the alkyl chain. This illustrated that the $NaGdF_4$:Yb,Er,Fe nanoparticles were coated with OA before $mSiO_2$ coating. In the FTIR spectrum of UCNPs@$mSiO_2$-COOH nanoparticles, the stretching vibration peaks of the hydroxyl group appeared from 3000 to 4000 cm^{-1}, the Si—O—Si bending vibration peak appeared at 459 cm^{-1}, and the asymmetric and symmetric stretching vibration peaks of Si—O were observed at 798 and 1079 cm^{-1}. In contrast, the stretching vibration peaks of Si—OH appeared at 963 cm^{-1}, and the vibration peaks of —CH_2 and —CH_3 appeared at 2924 and 2854 cm^{-1}. These findings demonstrated that the nanoparticles were successfully modified by silica (Cao et al., 2015). In addition, the peak at 1702 cm^{-1} corresponded to the C═O stretching vibration, indicating that the carboxyl group was successfully modified on the silica surface (Qian et al., 2014). The above-mentioned results indicated that UCNPs@$mSiO_2$ core-shell structure with carboxyl group modification was successfully prepared.

3.2.4. UV–vis spectroscopy

After successfully coating the mesoporous silica and modifying the carboxyl group, the absorption spectra of Ce6, DOX, UCNPs, UCNPs@$mSiO_2$, UCNPs@Ce6@$mSiO_2$, and UCNPs@Ce6@$mSiO_2$-DOX were measured using a UV–visible absorption spectrometer; the results are shown in Fig. 8. The photosensitizer Ce6 had obvious absorption peaks in the range of 338–434 nm and 620–660 nm, while the chemotherapeutic drug DOX had obvious absorption peaks in the range of 408–559 nm. There was no obvious absorption peak in the UV–vis absorption spectra of UCNPs and UCNPs@$mSiO_2$; however, after Ce6 was embedded in the mesoporous silica layer, obvious absorption peaks appeared at 412 and 664 nm, which were consistent with those of Ce6, indicating that Ce6 was successfully loaded onto the silicon dioxide layer. After DOX was also loaded, an absorption peak appeared at 504 nm, which was consistent with the DOX absorption peak range.

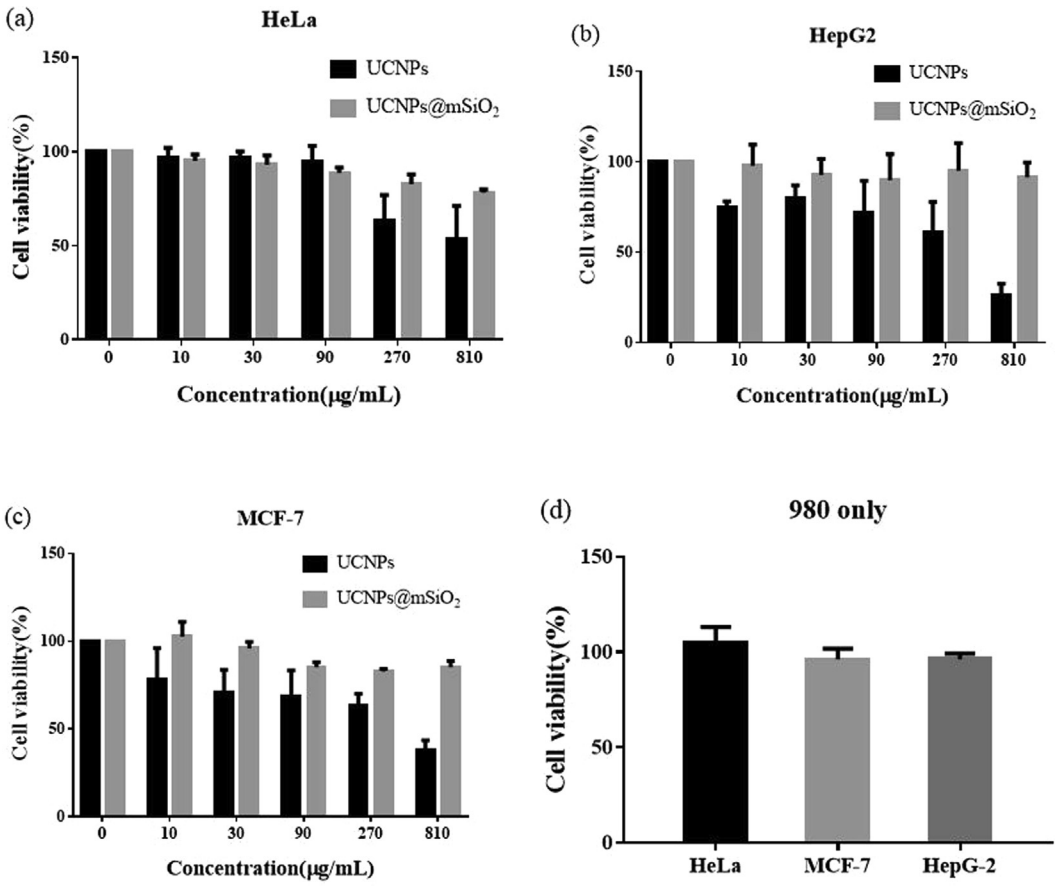

Fig. 11 Toxicity of UCNPs and UCNPs@$mSiO_2$ against (a) HeLa, (b) MCF-7, and (c) HepG2 cells. (d) Toxicity of infrared irradiation at 980 nm (2 W/cm^2, 10 min) against HeLa, MCF-7, and HepG2 cells.

3.2.5. UCL analysis

Fig. 9 shows the UCL spectrum upon excitation with NIR at 980 nm; UCNPs showed emission peaks at 409, 530, 550, and 654 nm, corresponding to $^2H_{9/2}$-$^4I1_{5/2}$, $^2H_{11/2}$-$^4I1_{5/2}$, $^4S_{3/2}$-$^4I_{15/2}$, and $^4F_{9/2}$-$^4I_{15/2}$ energy level transitions, respectively (Bai et al., 2007; Song et al., 2011; Yao et al., 2017). After the mesoporous silica layer was coated, the locations and intensities of UCL emission peaks did not change significantly ($P > 0.05$), indicating that the microporous silica coating had little effect on the luminescence UCNPs. After Ce6 loading, the fluorescence intensities at 530 and 550 nm did not change notably ($P > 0.05$), but the emission at 409 and 654 nm was significantly weakened (in the inset) ($P < 0.01$). These two emission peaks overlapped with the absorption peaks of Ce6 (Fig. 8), which indicated that fluorescence resonance energy transfer (FRET) may have occurred (Hu et al., 2019). After further loading DOX, the fluorescence intensities at 530 and 550 nm decreased. This might be due to the excessive loading of DOX on the surface of the nanoparticles, which caused a reduction in the NIR absorbed by the UCNP core. In contrast, as shown in Fig. 8, DOX showed light absorption at 408–559 nm, which overlapped with the green emission of UCNPs. Therefore, FRET may have also occurred, further resulting in a reduction in the emission intensity.

3.3. Drug delivery

As a PDT-chemo combined therapy drug delivery system, the Ce6 and DOX cargo in UCNPs@Ce6@$mSiO_2$-DOX is of great significance for the cancer cell-killing effect.

To detect Ce6 and DOX loading on the nanoplatform, the loading rate of Ce6 and DOX was determined using a standard curve. As shown in Fig. 10a, results showed that the loading rates of Ce6 and DOX reached 28.58 ± 0.85% and 87.53 ± 5 .53%, respectively. The high loading rates of Ce6 and DOX indicate the feasibility of subsequent PDT-chemo combined therapy.

To explore whether the nanomaterial can effectively release DOX in an acidic tumor microenvironment, the release of DOX was first measured in PBS at different pH values. A dialysis bag and UV–vis spectrophotometer were used to measure the DOX release in solution. As observed from Fig. 10b, the DOX release rate of UCNPs@Ce6@$mSiO_2$-DOX nanomaterials was relatively slow in a neutral solution (pH = 7.4); 17.5% after 24 h, and it stabilized at 24.4% after 72 h. By contrast, in an acidic environment (pH = 5.0), DOX release rate increased significantly ($P < 0.01$), reaching 57.5% within 24 h, and stabilizing at 85.3% after 72 h. The above-mentioned results demonstrated that the nanoplatform could effectively release

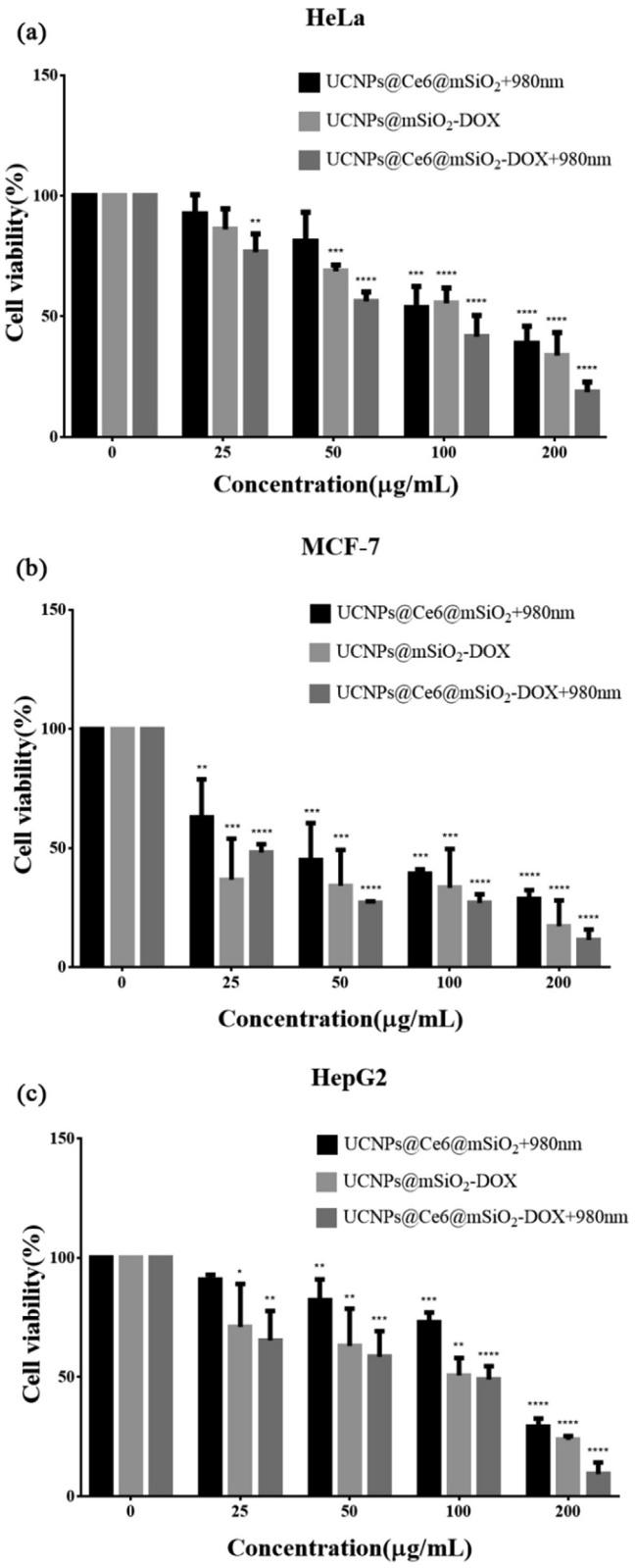

Fig. 12 PDT, chemotherapy, and PDT-chemotherapy combination applied to (a) HeLa, (b) MCF-7, and (c) HepG2 cells (*$p < 0.05$; **$p < 0.01$; ***$p < 0.001$; ****$p < 0.0001$).

DOX in an acidic environment, but only a small amount could be released in a neutral environment. This is because carboxyl groups increase the negative surface charge of the microporous silica shell, making it suitable for loading the weakly basic drug DOX (Li et al., 2016). Under physiological conditions (pH = 7.4), UCNPs@Ce6@$mSiO_2$ nanoparticles can maintain the electrostatic interaction between DOX molecules and carboxyl groups. However, in an acidic environment (such as a cancer microenvironment), the electrostatic interaction between nanoparticles and DOX decreases and the electrostatic repulsion enhances; therefore, DOX release increases (Xie et al., 2013).

Under NIR irradiation at 980 nm, $NaGdF_4$:Yb,Er,Fe UCNPs can emit strong green light. This fluorescence can further excite the photosensitizer Ce6 to produce ROS, which can enhance the effect of PDT treatment in cancer. ROS generation on the nanomaterial surface is the key in PDT, as the degree of DPBF degradation by ROS is used to evaluate the generation of ROS. As observed from Fig. 9c, DPBF in the solution was not degraded upon exposure to NIR irradiation. $NaGdF_4$:Yb,Er,Fe@$mSiO_2$ did not generate ROS.

However, when $NaGdF_4$:Yb,Er@Ce6@$mSiO_2$ nanomaterials were irradiated at 980 nm, the relative fluorescence intensity of DPBF decreased to 74.5% in 15 min and the degradation rate reached 25.5%. For $NaGdF_4$:Yb,Er,Fe@Ce6@$mSiO_2$ nanocarriers, the fluorescence intensity of DPBF reduced to 22.2% and the degradation rate reached 77.8%. The above-mentioned results illustrate that UCNPs@Ce6@$mSiO_2$ can effectively generate ROS under NIR irradiation, and Fe^{3+} doping can effectively increase the fluorescence intensity, thereby enhancing the production of active oxygen. These findings demonstrate that the nanoplatform has a high DOX and Ce6-loading capacity, DOX can be effectively released in the cancer microenvironment, and Ce6 generates a large amount of ROS under 980 nm NIR irradiation.

3.4. Killing effects on cancer cells

3.4.1. Cytotoxicity in the darkness and under 980 nm infrared light irradiation

To clarify the cytotoxic effects of UCNPs before and after mesoporous silica shell coating, MTT tests were performed using different cell lines treated with nanomaterials at concentrations of 0, 10, 30, 90, 270, and 810 μg/mL. As observed from Fig. 11, the viabilities of HeLa, MCF-7, and HepG2 cells treated with 10 μg/mL nanomaterials were about 96.9, 77.9, and 74.8%, respectively. As the nanomaterial concentration increased, the viabilities of the cancer cells decreased remarkably. When nanomaterial concentration reached 810 μg/mL, the average survival rates of the three cancer cell lines declined to 53.4, 37.6, and 26.0%, respectively. The viabilities of HeLa, MCF-7 and HepG2 cells exhibited obvious dose-effect manner. Cell viability decreases when the dose (or concentration) of the nanomaterials is increased. The toxicity was probably caused by OA, which is toxic to many cells in the human body at high concentrations (Fermor et al., 1992).

After coating with mesoporous silica, although the UCNP nanoplatform still exhibited slight cytotoxicity at high concentrations, the overall cell activity was significantly enhanced ($P < 0.01$). Even at a concentration of 810 μg/mL, cell viability was maintained at approximately 80%. This was possibly because water-soluble silica has excellent photochemical stability and negligible cytotoxicity (Yang and Li, 2020), which substantially reduces the cytotoxicity of nanocarriers. This demonstrates that the silica coating can effectively reduce the cytotoxicity of oleic acid-modified nanoparticles, thereby improving the biocompatibility of nanomaterials.

As the photodynamic analysis required NIR irradiation at 980 nm, the toxicity of NIR irradiation at 980 nm (2 W/cm^2) on HeLa, MCF-7, and HepG2 cells was evaluated. The results are shown in Fig. 11(d). We observed that NIR irradiation at 980 nm did not cause obvious cytotoxicity to the three cell lines, and the viabilities of all cells were above 95%.

3.4.2. UCNPs@Ce6@$mSiO_2$-DOX nanoplatform for PDT-chemotherapy of cancer cells

Fig. 12 shows the toxicity to HeLa, MCF-7 and HepG2 cells in the PDT group (UCNPs@Ce6@$mSiO_2$ + 980 nm), chemotherapy group (UCNPs@$mSiO_2$-DOX), and PDT-chemotherapy combination group (UCNPs@Ce6@$mSiO_2$-DOX + 980 nm), respectively. It can be observed from the figure that all the three experimental groups showed significant dose-effect relationship and high cancer cell toxicity ($P < 0.01$). At a concentration of 200 μg/mL, the viabilities of HeLa, MCF-7, and HepG2 cells in the PDT group decreased to 38.9, 28.6, and 29.3%, respectively; in the chemotherapy group, the cell viabilities declined to 33.7, 17.1, and 23.7%, respectively; in the PDT-chemotherapy combined group, the cell viabilities dropped to 18.5, 11.4, and 9.3%, respectively. Compared with those in the control group, the differences were statistically significant ($P < 0.01$). It is worth noting that under the same dose, the cell viability in the PDT-chemotherapy combined group was significantly lower than that in the other groups ($P < 0.0001$). This demonstrates that the UCNPs@Ce6@$mSiO_2$-DOX nanoplatform successfully combines the two treatment methods, at the same drug concentration. The nanoplatform has a strong killing capability against cancer cells in PDT-chemotherapy combination therapy.

Based on the previous analysis, we propose the basic principle of UCNPs@Ce6@$mSiO_2$-DOX nanoplatform for PDT-chemotherapy combination in the treatment of cancer cells. In a typical PDT treatment, when the UCNPs@Ce6@$mSiO_2$-DOX nanoplatform is irradiated at 980 nm, UCNPs are excited and can emit green light to excite the photosensitizer Ce6, which can produce $^1O_2$ and ROS (Agostinis et al., 2011; Zhang et al., 2015; Zhang et al., 2017a). These intracellular ROS could easily damage biomolecules by causing oxidative stress or via direct reaction with DNA, leading to apoptosis (Tang et al., 2018). In contrast, due to the unique acidic environment in cancer cells, DOX carried by the UCNPs@Ce6@$mSiO_2$-DOX nanoplatform can be effectively released, and DOX can effectively promote cancer cell apoptosis by inhibiting DNA and RNA synthesis (Zhang et al., 2017b). It also can directly act on the nucleus and lead to apoptosis. This indicates that the UCNPs@Ce6@$mSiO_2$-DOX nanoplatform can successfully achieve the combined therapy of PDT and chemotherapy to kill cancer cells.

4. Conclusions

In this study, a UCNPs@Ce6@$mSiO_2$-DOX PDT/chemotherapy nanoplatform was successfully constructed. The nanoplatform has a high Ce6 and DOX loading rate. Under 980 nm laser irradiation, the nanoplatform emits bright green fluorescence, which can activate the photosensitizer Ce6 to effectively generate ROS. The loaded DOX can also be released under acidic conditions into the cancer microenvironment. The UCNPs@Ce6@$mSiO_2$-DOX treatment has stronger cytotoxic effects against HeLa, MCF-7, and HepG2 cells than single PDT (UCNPs@Ce6@$mSiO_2$) or single chemotherapy (UCNPs@$mSiO_2$-DOX). This nanoplatform, which combines PDT and chemotherapy, can significantly improve the treatment efficiency of cancer cells and exhibit excellent application potential in cancer treatment.

Declaration of Competing Interest

The authors declare that they have no known competing financial interests or personal relationships that could have appeared to influence the work reported in this paper.

Acknowledgments

This work was supported by the National Natural Science Foundation of China (grant number 82173486) and the Natural Sciences Foundation of Tianjin City of China (grant number 12JCYBJC19100).

Appendix A. Supplementary material

Supplementary data to this article can be found online at https://doi.org/10.1016/j.arabjc.2022.103934.

References

Agostinis, P., Berg, K., Cengel, K.A., Foster, T.H., Girotti, A.W., Gollnick, S.O., Hahn, S.M., Hamblin, M.R., Juzeniene, A., Kessel, D., Korbelik, M., Moan, J., Mroz, P., Nowis, D., Piette, J., Wilson, B.C., Golab, J., 2011. Photodynamic therapy of cancer: an update. CA Cancer J. Clin. 61, 250–281. https://doi.org/10.3322/caac.20114.

Bai, X., Song, H.W., Pan, G.H., Lei, Y.Q., Wang, T., Ren, X.G., Lu, S.Z., Dong, B., Dai, Q.L., Fan, L., 2007. Size-dependent upconversion luminescence in Er^{3+}/Yb^{3+}-codoped nanocrystalline yttria: Saturation and thermal effects. J. Phys. Chem. C 111, 13611–13617. https://doi.org/10.1021/jp070122e.

Bray, F., Jemal, A., Grey, N., Ferlay, J., Forman, D., 2012. Global cancer transitions according to the Human Development Index (2008–2030): a population-based study. Lancet Oncol. 13, 790–801. https://doi.org/10.1016/s1470-2045(12)70211-5.

Cao, P., Ni, Y., Zou, R., Zhang, L., Yue, D., 2015. Enhanced catalytic properties of rhodium nanoparticles deposited on chemically modified SiO_2 for hydrogenation of nitrile butadiene rubber. RSC Adv. 5, 3417–3424. https://doi.org/10.1039/c4ra11711e.

Cho, I.-H., Shim, M.K., Jung, B., Jang, E.H., Park, M.-J., Kang, H. C., Kim, J.-H., 2017. Heat shock responsive drug delivery system based on mesoporous silica nanoparticles coated with temperature sensitive gatekeeper. Micropor. Mesopor. Mater. 253, 96–101. https://doi.org/10.1016/j.micromeso.2017.06.042.

Chuai, X.H., Guo, X.Y., Liu, X.H., He, G.H., Zheng, K.Z., He, C.F., Qin, W.P., 2015. Bifunctional $NaGdF_4$:Yb, Er, Fe nanocrystals with the enhanced upconversion fluorescence. Opt. Mater. 44, 13–17. https://doi.org/10.1016/j.optmat.2015.02.019.

Deng, Y., Wang, H., Gu, W., Li, S., Xiao, N., Shao, C., Xu, Q., Ye, L., 2014. Ho^{3+} doped $NaGdF_4$ nanoparticles as MRI/optical probes for brain glioma imaging. J. Mater. Chem. B 2, 1521–1529. https://doi.org/10.1039/c3tb21613f.

Dong, J., Wang, K., Sun, L., Sun, B., Yang, M., Chen, H., Wang, Y., Sun, J., Dong, L., 2018. Application of graphene quantum dots for simultaneous fluorescence imaging and tumor-targeted drug delivery. Sens. Actuators B: Chem. 256, 616–623. https://doi.org/10.1016/j.snb.2017.09.200.

Fermor, B.F., Masters, J.R., Wood, C.B., Miller, J., Apostolov, K., Habib, N.A., 1992. Fatty acid composition of normal and malignant cells and cytotoxicity of stearic, oleic and sterculic acids in vitro. Eur. J. Cancer 28A, 1143–1147. https://doi.org/10.1016/0959-8049(92)90475-h.

Grzyb, T., Mrowczynska, L., Szczeszak, A., Sniadecki, Z., Runowski, M., Idzikowski, B., Lis, S., 2015. Synthesis, characterization, and cytotoxicity in human erythrocytes of multifunctional, magnetic, and luminescent nanocrystalline rare earth fluorides. J. Nanopart. Res. 17, 399. https://doi.org/10.1007/s11051-015-3191-2.

Gui, W., Zhang, J., Chen, X., Yu, D., Ma, Q., 2017. N-Doped graphene quantum dot@mesoporous silica nanoparticles modified with hyaluronic acid for fluorescent imaging of tumor cells and drug delivery. Mikrochim. Acta 185, 66. https://doi.org/10.1007/s00604-017-2598-0.

Hu, J., Shi, J., Gao, Y., Yang, W., Liu, P., Liu, Q., He, F., Wang, C., Li, T., Xie, R., Zhu, J., Yang, P., 2019. 808 nm near-infrared light-excited UCNPs@$mSiO_2$-Ce6-GPC3 nanocomposites for photodynamic therapy In liver cancer. Int. J. Nanomed. 14, 10009–10021. https://doi.org/10.2147/IJN.S221496.

Jiang, R., Zhu, H.Y., Chen, H.H., Yao, J., Fu, Y.Q., Zhang, Z.Y., Xu, Y.M., 2014. Effect of calcination temperature on physical parameters and photocatalytic activity of mesoporous titania spheres using chitosan/poly(vinyl alcohol) hydrogel beads as a template. Appl. Surf. Sci. 319, 189–196. https://doi.org/10.1016/j.apsusc.2014.06.185.

Li, F.Y., Gu, W., Wang, H., Qi, Y.Z., Deng, Y.L., Xiao, N., Liu, Y., Xu, Q.Y., Ye, L., 2013. Effect of surface functionalities on relaxometric properties of MR contrast agents based on $NaGdF_4$ nanoparticles. RSC Adv. 3, 5386–5392. https://doi.org/10.1039/c3ra22505d.

Li, J., Du, X., Zheng, N., Xu, L., Xu, J., Li, S., 2016. Contribution of carboxyl modified chiral mesoporous silica nanoparticles in delivering doxorubicin hydrochloride in vitro: pH-response controlled release, enhanced drug cellular uptake and cytotoxicity. Colloids Surf. B Biointerfaces 141, 374–381. https://doi.org/10.1016/j.colsurfb.2016.02.009.

Li, Q., Zhou, Y., He, W., Ren, X., Zhang, M., Jiang, Y., Zhou, Z., Luan, Y., 2021. Platelet-armored nanoplatform to harmonize janus-faced IFN-gamma against tumor recurrence and metastasis. J. Control. Release 338, 33–45. https://doi.org/10.1016/j.jconrel.2021.08.020.

Liu, C., Qi, Y., Qiao, R., Hou, Y., Chan, K., Li, Z., Huang, J., Jing, L., Du, J., Gao, M., 2016. Detection of early primary colorectal cancer with upconversion luminescent NP-based molecular probes. Nanoscale 8, 12579–12587. https://doi.org/10.1039/c5nr07858j.

Liu, Y., Si, Y., Di, M., Tang, D., Meng, L., Cui, B., 2021. A novel microwave stimulus remote-controlled anticancer drug release system based on Janus TiO_{2-x}&$mSiO_2$ nanocarriers. Mater. Sci. Eng. C Mater. Biol. Appl. 123, 111968. https://doi.org/10.1016/j.msec.2021.111968.

Lu, F., Wu, S.H., Hung, Y., Mou, C.Y., 2009. Size effect on cell uptake in well-suspended, uniform mesoporous silica nanoparticles. Small 5, 1408–1413. https://doi.org/10.1002/smll.200900005.

Lu, J., Liong, M., Zink, J.I., Tamanoi, F., 2007. Mesoporous silica nanoparticles as a delivery system for hydrophobic anticancer drugs. Small 3, 1341–1346. https://doi.org/10.1002/smll.200700005.

Nagasubramanian, R., Innocenti, F., Ratain, M.J., 2003. Pharmacogenetics in cancer treatment. Annu. Rev. Med. 54, 437–452. https://doi.org/10.1146/annurev.med.54.101601.152352.

Qian, W., Wei, W., Hong, M., Jianfeng, C., Guangwen, C., Haikui, Z., 2014. Microwave assisted synthesis of ZnPc-COOH and SiO_2 / ZnPc-COOH nanopaticles: Singlet oxygen production and photocatalytic property. Colloids Surf. A: Physicochem. Eng. Aspects. 443, 52–59. https://doi.org/10.1016/j.colsurfa.2013.10.056.

Ramasamy, P., Chandra, P., Rhee, S.W., Kim, J., 2013. Enhanced upconversion luminescence in $NaGdF_4$:Yb, Er nanocrystals by F^{e3+} doping and their application in bioimaging. Nanoscale. 5, 8711–8717. https://doi.org/10.1039/c3nr01608k.

Shen, J.W., Wang, J.N., Kong, D.L., Yan, X.P., 2014. Sub-20 nm sandwich-structured $NaGdF_4$:Yb/Tm@$NaLuF_4$:Yb/Tm@$NaYF_4$ nanocrystals for in vivo upconversion luminescence/computed tomography imaging. RSC Adv. 4, 5088–5091. https://doi.org/10.1039/c3ra46885b.

Slowing, I.I., Trewyn, B.G., Giri, S., Lin, V.S.Y., 2007. Mesoporous silica nanoparticles for drug delivery and biosensing applications. Adv. Funct. Mater. 17, 1225–1236. https://doi.org/10.1002/adfm.200601191.

Song, Y.L., Tian, Q.W., Zou, R.J., Chen, Z.G., Yang, J.M., Hu, J.Q., 2011. Phase and luminescent intensity control of hydrophilic rare-earth up-converting nanophosphors prepared by one-pot solvothermal synthesis. J. Alloy. Compd. 509, 6539–6544. https://doi.org/10.1016/j.jallcom.2011.03.122.

Sung, H., Ferlay, J., Siegel, R.L., Laversanne, M., Soerjomataram, I., Jemal, A., Bray, F., 2021. Global Cancer Statistics 2020: GLOBOCAN Estimates of Incidence and Mortality Worldwide for 36 Cancers in 185 Countries. CA Cancer J. Clin. 71, 209–249. https://doi.org/10.3322/caac.21660.

Tang, J., Chen, L., Li, J., Wang, Z., Zhang, J., Zhang, L., Luo, Y., Wang, X., 2015. Selectively enhanced red upconversion luminescence and phase/size manipulation via Fe^{3+} doping in $NaYF_4$:Yb, Er nanocrystals. Nanoscale 7, 14752–14759. https://doi.org/10.1039/c5nr04125b.

Tang, X.L., Jing, F., Lin, B.L., Cui, S., Yu, R.T., Shen, X.D., Wang, T.W., 2018. pH-responsive magnetic mesoporous silica-based nanoplatform for synergistic photodynamic therapy/chemotherapy. ACS Appl. Mater. Interfaces 10, 15001–15011. https://doi.org/10.1021/acsami.7b19797.

Teng, B., Han, Y., Zhang, X., Xiao, H., Yu, C., Li, H., Cheng, Z., Jin, D., Wong, K.L., Ma, P., Lin, J., 2018. Phenanthriplatin(iv) conjugated multifunctional up-converting nanoparticles for drug delivery and biomedical imaging. J. Mater. Chem. B 6, 5059–5068. https://doi.org/10.1039/c8tb01034j.

Tian, J., Shao, Q., Zhao, J., Pan, D., Dong, M., Jia, C., Ding, T., Wu, T., Guo, Z., 2019. Microwave solvothermal carboxymethyl chitosan templated synthesis of TiO_2/ZrO_2 composites toward enhanced photocatalytic degradation of Rhodamine B. J. Colloid Interface Sci. 541, 18–29. https://doi.org/10.1016/j.jcis.2019.01.069.

Trewyn, B.G., Nieweg, J.A., Zhao, Y., Lin, V.S.Y., 2008. Biocompatible mesoporous silica nanoparticles with different morphologies for animal cell membrane, penetration. Chem. Eng. J. 137, 23–29. https://doi.org/10.1016/j.cej.2007.09.045.

Vetrone, F., Naccache, R., Mahalingam, V., Morgan, C.G., Capobianco, J.A., 2009. Upconverting nanoparticles: The active-Core/Active-Shell approach: A strategy to enhance the upconversion luminescence in lanthanide-doped nanoparticles (Adv. Funct. Mater. 18/2009). Adv. Funct. Mater. 19, 7652–7657. https://doi.org/10.1002/adfm.200990081.

Vivero-Escoto, J.L., Slowing, I.I., Trewyn, B.G., Lin, V.S., 2010. Mesoporous silica nanoparticles for intracellular controlled drug delivery. Small 6, 1952–1967. https://doi.org/10.1002/smll.200901789.

Wei, W., Jiao, J., Liu, Y., Liu, L., Lv, B., Li, Z., Gai, S., Tang, J., 2019. Effect of the Fe^{3+} concentration on the upconversion luminescence in $NaGdF_4$:Yb^{3+}, Er^{3+} nanorods prepared by a hydrothermal method. J. Mater. Sci. 54, 13200–13207. https://doi.org/10.1007/s10853-019-03818-9.

Wu, Y., Yang, D., Kang, X., Li, C., Lin, J., 2013. Facile fabrication of water-soluble Ln^{3+}-doped β-$NaGdF_4$ nanocrystals (Ln = Ce, Tb, Eu, Dy) with multicolor luminescence and magnetic properties. Mater. Res. Bull. 48, 2843–2849. https://doi.org/10.1016/j.materresbull.2013.04.014.

Xie, M., Shi, H., Li, Z., Shen, H., Ma, K., Li, B., Shen, S., Jin, Y., 2013. A multifunctional mesoporous silica nanocomposite for targeted delivery, controlled release of doxorubicin and bioimaging. Colloids Surf. B Biointerfaces 110, 138–147. https://doi.org/10.1016/j.colsurfb.2013.04.009.

Xu, J., Gai, S., Ma, P., Dai, Y., Yang, G., He, F., Yang, P., 2014. Gadolinium fluoride mesoporous microspheres: controllable synthesis, materials and biological properties. J. Mater. Chem. B 2, 1791–1801. https://doi.org/10.1039/c3tb21465f.

Yang, S., Li, Y., 2020. Fluorescent hybrid silica nanoparticles and their biomedical applications. Wiley Interdiscip. Rev. Nanomed. Nanobiotechnol. 12, e1603. https://doi.org/10.1002/wnan.1603.

Yao, J., Zhao, F., Pan, C., Zhuang, J., 2017. Controlled synthesis of $BaYF_5$:Er^{3+}, Yb^{3+} with different morphology for the enhancement of upconversion luminescence. Nanoscale Res. Lett. 12, 633. https://doi.org/10.1186/s11671-017-2390-4.

Yin, M., Ju, E., Chen, Z., Li, Z., Ren, J., Qu, X., 2014. Upconverting nanoparticles with a mesoporous TiO_2 shell for near-infrared-triggered drug delivery and synergistic targeted cancer therapy. Chemistry 20, 14012–14017. https://doi.org/10.1002/chem.201403733.

Zhang, D., Wu, M., Zeng, Y., Wu, L., Wang, Q., Han, X., Liu, X., Liu, J., 2015. Chlorin e6 conjugated poly(dopamine) nanospheres as PDT/PTT dual-modal therapeutic agents for enhanced cancer therapy. ACS Appl. Mater. Interfaces 7, 8176–8187. https://doi.org/10.1021/acsami.5b01027.

Zhang, D., Zheng, A., Li, J., Wu, M., Cai, Z., Wu, L., Wei, Z., Yang, H., Liu, X., Liu, J., 2017a. Tumor microenvironment activable self-assembled DNA hybrids for pH and redox dual-responsive chemotherapy/PDT treatment of hepatocellular carcinoma. Adv. Sci. 4, 1600460. https://doi.org/10.1002/advs.201600460.

Zhang, H., Wu, Y., Wang, J., Tang, Z., Ren, Y., Ni, D., Gao, H., Song, R., Jin, T., Li, Q., Bu, W., Yao, Z., 2018. In vivo MR imaging of glioma recruitment of adoptive T-cells labeled with NaGdF4 -TAT nanoprobes. Small 14, 1702951. https://doi.org/10.1002/smll.201702951.

Zhang, M., Qin, X., Xu, W., Wang, Y., Song, Y., Garg, S., Luan, Y., 2021. Engineering of a dual-modal phototherapeutic nanoplatform for single NIR laser-triggered tumor therapy. J. Colloid Interface Sci. 594, 493–501. https://doi.org/10.1016/j.jcis.2021.03.050.

Zhang, M., Qin, X., Zhao, Z., Du, Q., Li, Q., Jiang, Y., Luan, Y., 2022. A self-amplifying nanodrug to manipulate the Janus-faced nature of ferroptosis for tumor therapy. Nanoscale Horiz. 7, 198–210. https://doi.org/10.1039/d1nh00506e.

Zhang, Y., Huang, F., Ren, C., Yang, L., Liu, J., Cheng, Z., Chu, L., Liu, J., 2017b. Targeted chemo-photodynamic combination platform based on the DOX prodrug nanoparticles for enhanced cancer therapy. ACS Appl. Mater. Interfaces 9, 13016–13028. https://doi.org/10.1021/acsami.7b00927.

Zhou, L., Chen, Z., Dong, K., Yin, M., Ren, J., Qu, X., 2014. DNA-mediated biomineralization of rare-earth nanoparticles for simultaneous imaging and stimuli-responsive drug delivery. Biomaterials 35, 8694–8702. https://doi.org/10.1016/j.biomaterials.2014.06.034.

Zhou, S., Shang, Q., Wang, N., Li, Q., Song, A., Luan, Y., 2020. Rational design of a minimalist nanoplatform to maximize immunotherapeutic efficacy: Four birds with one stone. J. Control. Release 328, 617–630. https://doi.org/10.1016/j.jconrel.2020.09.035.